Published in final edited form as:
ACS Nano. 2012 July 24; 6(7): 6150–6164. doi:10.1021/nn301495k.

Silicon Nanowires with High-k Hafnium Oxide Dielectrics for Sensitive Detection of Small Nucleic Acid Oligomers

Brian R. Dorvel[3,4,*], **Bobby Reddy Jr**[1,4,*], **Jonghyun Go**[5], **Carlos Duarte Guevara**[1,4], **Eric Salm**[2,4], **Muhammad Ashraful Alam**[5], and **Rashid Bashir**[1,2,4,^]

[1]Department of Electrical and Computer Engineering, University of Illinois at Urbana Champaign, Urbana, Illinois, 61801

[2]Department of Bioengineering, University of Illinois at Urbana Champaign, Urbana, Illinois, 61801

[3]Department of Biophysics and Computational Biology, University of Illinois at Urbana Champaign, Urbana, Illinois, 61801

[4]Micro and Nanotechnology Lab, University of Illinois at Urbana Champaign, Urbana, Illinois, 61801

[5]School of Electrical and Computer Engineering, Purdue University, West Lafayette, IN. 47906

Abstract

Nanobiosensors based on silicon nanowire field effect transistors offer advantages of low cost, label-free detection, and potential for massive parallelization. As a result, these sensors have often been suggested as an attractive option for applications in Point-of-care (POC) medical diagnostics. Unfortunately, a number of performance issues such as gate leakage and current instability due to fluid contact, have prevented widespread adoption of the technology for routine use. High-k dielectrics, such as hafnium oxide (HfO_2), have the known ability to address these challenges by passivating the exposed surfaces against destabilizing concerns of ion transport. With these fundamental stability issues addressed, a promising target for POC diagnostics and SiNWFET's has been small oligonucleotides, more specifically microRNA (miRNA). MicroRNA's are small RNA oligonucleotides which bind to messenger RNA's, causing translational repression of proteins, gene silencing, and expressions are typically altered in several forms of cancer. In this paper, we describe a process for fabricating stable HfO_2 dielectric based silicon nanowires for biosensing applications. Here we demonstrate sensing of single stranded DNA analogues to their microRNA cousins using miR-10b and miR-21 as templates, both known to be upregulated in breast cancer. We characterize the effect of surface functionalization on device performance using the miR-10b DNA analogue as the target sequence and different molecular weight poly-l-lysine as the functionalization layer. By optimizing the surface functionalization and fabrication protocol, we were able to achieve <100fM detection levels of miR-10b DNA analogue, with a theoretical limit of detection of 1fM. Moreover, the non-complementary DNA target strand, based on miR-21, showed very little response, indicating a highly sensitive and highly selective biosensing platform.

^Corresponding author: rbashir@illinois.edu.
*Denotes Equal Contribution

Supporting Information Available: The measurement of leakage current through the device to the fluid gate, the transfer curves for the silicon nanowire functionalization process with PLL and probe molecules, changes in surface potential for the different functionalization chemistries for nanowires and nanoplates, and the surface potential changes to DNA concentration for nanoplates are included. This information is available free of charge *via* the Internet at http://pubs.acs.org.

Keywords

nanowire; miRNA; DNA; hafnium oxide; surface functionalization; sensing

Point-of-care (POC) diagnostics has emerged as an exciting field where devices can provide rapid, cheap, and accurate results in a portable format. Such diagnostic devices have the potential to provide critical patient information more rapidly at cheaper costs than instruments in centralized lab facilities, reducing the turnaround time for results in critical care situations.[1, 2] Moreover, POC diagnostics can present patients with more control of their own therapy,[3] leading to greater patient satisfaction and improved clinical outcome.[4] In particular, treatment for various forms of cancer could benefit greatly from such POC devices. As our knowledge of cancer pathways rapidly grows, important indicators of cancer have been revealed, including changes in the genome, exome, transcriptome, and expression levels of several cancer biomarkers such as proteins and microRNA (miRNA). Devices that can rapidly detect cancer biomarkers in a rapid, accurate, multiplexed, and cost-efficient fashion would revolutionize cancer treatment, allowing for better evaluation of the efficacy of treatment, earlier detection of cancer, and de-convolution of the complex pathways that result in cancer.

Adaption of the ubiquitous field effect transistor (FET) technology has been proposed as a possible core technology for the sensing component of POC devices, due to the potential for low per unit cost, label-free detection, and amenability for scale-up and integration with signal processing electronics. Electrochemical detection methodologies based upon ion sensitive field effect transistor's (ISFETs) have been studied extensively,[5] including its use as biosensors (bioFET).[6–10] The performance of ISFET and bioFET relies on the charge of a binding biological analyte over the gate insulator of the FET, which induces changes in the source-drain current of the device. This allows for label-free, ultrasensitive, and rapid detection of relevant biological analytes.

Silicon nanowire FET devices (SiNWFETs), where the silicon channel has thicknesses and diameters in the tens of nanometers or less have further enhanced properties. Using SiNWFETs, researchers have demonstrated detection of biological analytes such as proteins,[11–16] DNA,[17–20] RNA,[21] ions,[22] and other small molecules[23] down to fM concentrations. The increased sensitivity of these devices is mainly attributed to the increased gate control of the silicon channel due to a higher surface area to volume ratio. Thus, silicon nanowires show promise in cancer diagnosis, since various cancer biomarkers may exist in small concentrations throughout the disease pathogenesis. Silicon nanowire FETs fabricated with "top-down" techniques[17, 24–30] are particularly attractive, due to CMOS compatibility and high amenability for scale-up. However, though nanowire technology has existed for over a decade, several issues have prevented the technology from maturation into fully fledged POC products. Various issues have arisen regarding device stability in fluid such as measurement drift,[31] leakage paths through the sensing dielectric, high background l/f noise,[32–34] and lack of repeatability. Silicon oxide, the traditional top gate dielectric, is one of the main culprits behind several of these issues, due to its relatively low dielectric constant, low pH buffering capacity, and susceptibility of gradual charge incorporation by ion diffusion when exposed to fluid.[35, 36] To circumvent some of these issues, researchers have turned to high-k materials, including aluminum oxide (Al_2O_3),[37] hafnium oxide (HfO_2),[38] and tantalum oxide (Ta_2O_5).[39] High-k materials enable high gate oxide capacitance values even with physically thicker gate oxides, allowing a reduction in leakage current. HfO_2 has arisen as a particularly promising dielectric for ISFET's and MOSFET's due to its stability on silicon and its acceptable bandgap and conduction band

offset values. It can be deposited by chemical vapor deposition and yields improved pH sensitivity.[40,41]

To date, however, there have been very few reports that offer detailed characterization and application of hafnium oxide-based FETs for biosensing applications. Annealing of HfO_2 has been shown to improve pH sensitivity in a two terminal EIS (electrolyte-insulator-semiconductor) capacitor using capacitance-voltage curves.[42] However, such a structure does not take advantage of the main desirable property for a FET, its intrinsic high current gain (high transconductance). In addition, HfO_2 deposited at high CVD temperatures for ISFETs lead to leakage paths in the silicon in high aspect ratio areas and results in higher roughness,[43] which is undesirable for a charge based biosensor. The demonstrated sensitivity for this structure was very low (biotin and streptavidin detected down to ~50ug/mL).[44] pH sensing has been demonstrated with a FET structure with encouraging near-Nernstian results, but no molecular sensing has been reported to date.[38]

Here we describe a process for fabricating robust HfO_2 based silicon nanoFET sensors for biological applications. We use atomic layer deposition (ALD) to form the hafnium oxide dielectric and a wet etch based process for releasing the device structures. Unlike CVD methodologies, ALD is more conformal and can be performed at lower deposition temperatures with better process control. Additionally, the wet etch based process for device release eliminates the possibility of RIE induced damage to the delicate dielectric layer. We have characterized in detail the properties of this low temperature deposition process and optimized subsequent annealing conditions to create a high quality dielectric. Moreover, we discuss the electrical and chemical advantages of the process, which include HfO_2 becoming an excellent wet etch stop for acid, alkali, and oxidizing chemistries. By thoroughly characterizing the HfO_2-silicon interface, we were able to produce a high quality gate dielectric layer, resulting in a device with high repeatability and low hysteresis in fluid. The devices are highly stable and robust, and show minimal drift over hours in fluid. As a result, we were able to achieve ~56mV/pH unit response for nanowire devices. We then demonstrate the sensitive detection of a DNA analogue sequence of microRNA, which can be highly important cancer biomarkers. MicroRNA's (miRNA's) are small RNA oligonucleotides which bind to messenger RNA's, causing translational repression of proteins and gene silencing. In this work we focus on sensing DNA analogues of miRNA's, with templates based upon miR-10b and miR-21, miRNA's commonly upregulated in breast cancer.[45–49] Moreover, miR-21 is found in a 4 fold higher concentration than miR-10b in normal tissue,[50] making miR-10b a harder analyte to detect even when upregulated. The devices were functionalized with different molecular weight poly-lysine strands and DNA probes specific to the miR-10b DNA analogue sequence. Different sensitivities for the different molecular weight poly-lysines were achieved for miR-10b, with lower sensitivity being achieved on the higher molecular weight polymer. Analysis of the layers showed lower probe density and higher roughness for the higher molecular weight layer of poly-l-lysine. The devices were able to achieve 100fM detection limits for the miR-10b DNA in comparison against a miR-21 non-complementary target, with a theoretical limit of detection of 1fM. Various characteristic features of these systematic set of experiments are interpreted and supported by well calibrated theoretical models.

Results & Discussion

One of the most important components of any silicon based FET is the gate dielectric and its interface with silicon. We chose HfO_2 because it currently satisfies the requirements demanded for CMOS integration. Atomic layer deposition was chosen as the method for forming the gate dielectric because of its self-limiting growth process, meaning the thickness is controlled by the number of deposition cycles, allowing accurate thickness control and

uniform step coverage. Moreover, due the reactive nature of the precursors, the temperature window for deposition is wide. However, the electrical and chemical properties of the film are temperature dependent as well. Before using HfO_2 as our gate dielectric we characterized the properties of the hafnium oxide layer as deposited and how the thermal treatments taken during our process affect the gate dielectric.

During the nanowire fabrication process, the hafnium oxide must be amenable to hydrofluoric acid wet etching in order to create the contact vias over the source-drain regions of the FET. The concentration of HF also must be gentle enough as to not deteriorate the photoresist leading us to use a 10:1 buffered oxide etchant (BOE) as the reagent. During the course of characterization, we observed ALD deposition temperatures >200°C resulted in a layer which would not etch in BOE solution. Layers deposited at <80°C etched very quickly and had deposition rates much larger than the limiting rate of ~1 Å/cycle. In our process we use a temperature of 120°C, which gave us a good compromise between etching rate and deposition rate.

The characterization of the deposition thickness *vs.* number of cycles was done using ellipsometry and is shown in Figure 1A. Here we assumed a simple bilayer stack of HfO_2 and Si, with refractive indices taken from the Sopra Material Library. By depositing ALD films between 10 and 90 cycles and measuring the thickness we were able to verify the deposition rate per cycle and estimate the interfacial oxide thickness. The overall thickness (T) of the film on silicon is related to the HfO_2 deposition cycle number (N_{HfO2}) by:

$$T(nm)=R_{dep}N_{HfO2}+t_{sio2}$$

where R_{dep} is the deposition rate and t_{sio2} the native oxide thickness. By fitting a line to the data in Figure 1A we get a deposition rate of 1.23 Angstroms per cycle and, if we extrapolate back to zero cycles, a native oxide thickness of 9 Angstroms. These results are within range of the reported growth rates of HfO_2[51, 52] and thickness of a chemically grown native oxide.[53]

After ALD of the hafnium oxide films, we investigated how annealing would affect the chemical and electrical properties of the gate dielectric. Annealing of the films is an important parameter in optimizing the electrical performance of the gate dielectric. HfO_2 begins to crystallize at temperatures >500°C, and the crystallization temperature is thickness dependent, increasing with decreasing thickness.[54] Crystallization, although helps increase the dielectric constant, is known to increase the leakage current through grain boundaries in MOS structures as well. Thus, leakage would be amplified even more in an aqueous setting where ions are even more mobile than with a top metal. During our process we decided to keep our anneal steps below 500°C in order to avoid excess leakage affects. First, we perform a rapid thermal process in Ar at 500°C for 60s to densify the gate dielectric. Then, after the deposition of the leads, we do a forming gas anneal ($Ar/10\%H_2$) at 450°C for 30 minutes to passivate interface traps and anneal the leads. This constitutes our basic annealing procedure on the gate dielectric.

To examine how the anneal steps affected the gate dielectric chemically, we subjected the annealed and unannealed films to various strong acid etchants such as acid piranha and SC2, as well as in 10:1 BOE. The etch rates for hafnium oxide annealed *vs.* unannealed are presented in Figure 1B. The films deposited at 120°C show etch susceptibility for all the etching solutions. Etch rates between 15–40 Angstroms per minute are achieved with the various etching parameters. After the rapid thermal anneal and forming gas treatments, the hafnium oxide becomes chemically inert. The ellipsometric thickness of the films only

changes by ~5 Angstroms for each of the etchants. We attribute the thickness change to a thin carbonaceous layer on top of the film which is subsequently removed during exposure to the etching solutions.

In order to determine how the annealing affects the system electrically, MOS capacitors were formed by sputtering 30nm TiN then 100nm Al on the HfO_2 and 100nm Al on the back of p-type silicon contact to create a capacitor with a structure shown in Figure 1D. High frequency capacitance-voltage curves were taken for as-deposited, RTP only, and RTP +forming gas HfO_2 substrates. The results for a 100 cycle ALD HfO_2 film are shown in Figure 1C. Each device was swept ten times to give insight into its stability. Using the high frequency capacitance we can extract parameters such as the oxide thickness, dielectric constant, effective charge, and flatband voltage. For a p-type MOS-C, the accumulation region of the C-V curve is observed when negative voltages are applied to the gate. The oxide capacitance (C_{ox}) is the high frequency capacitance when the device is biased for strong accumulation. If we assume the oxide is one entity, MOS-C acts like a single parallel-plate capacitor and C_{ox} is related to the total oxide thickness (t_{ox}) by:

$$C_{ox}=\frac{\varepsilon_0 K_{eff} A}{t_{ox}},$$

where ε_0 is the permittivity of free space, A the capacitor area, and K_{eff} the relative dielectric constant. From Figure 1C, we can see that C_{ox} increases as we perform the annealing procedures, indicating that Keff is increasing and thus producing a higher quality HfO_2 layer. As we anneal the samples, we also notice the flatband voltage of the MOSCap's shifts to more positive potentials and the drift (or variance) becomes minimized for the RTP and forming gas system. The flatband voltage (V_{fb}) for MOSCap's can be expressed as:

$$V_{fb}=\varphi_{MS}-\frac{Q_{EFF}}{C_{ox}}$$

where φ_{MS} is the work function difference between the metal and the semiconductor and Q_{EFF} is the effective oxide charge density, given by the sum of the oxide fixed charge (Q_F) mobile charge (Q_M), and oxide trapped charge (Q_{OT}) with $Q_{EFF} = Q_F + Q_M + Q_{OT}$. We extract the flatband voltage from the flatband capacitance by interpolating between the closest voltages around the flatband capacitance value. We then extract the variance and Q_{EFF} for each MOSCap under study from the flatband voltages for each curve. The Q_{EFF} and variances for each of anneals is found in the inset in Figure 1C. By annealing the substrates we eliminate most of the effective charge and variance in the system. This is probably due to the removal of dangling bonds in the oxides and passivation of interface traps at the HfO_2-SiO_2 and SiO_2-Si interfaces.[55]

To determine the dielectric constant of the annealed HfO_2, different cycle amounts of HfO_2 were deposited and C_{ox} determined. If we assume the dielectric is composed entirely of SiO_2 (since the dielectric constant is known) we can replace the K_{eff} in equation 1 with the dielectric constant of SiO_2 (3.9) and extract an equivalent oxide thickness (EOT) for the layer. An example of this is found in the inset of Figure 1D, along with the stack for the MOS capacitors. The EOT of the HfO_2 MOSCap's was plotted *versus* the ALD cycle number (N) and is shown in Figure 1D. The EOT is a combination of the HfO_2 thickness and dielectric constant with the interfacial oxide thickness and dielectric constant. It can be expressed in a linear form by:

$$EOT(N)=\left(\frac{3.9}{K}\right)R_{dep}N+t_{sio2}$$

The dielectric constant can be extracted from the slope of the line $\left(\frac{3.9}{K}\right)R_{dep}$ assuming the deposition rate is known, which we extracted from ellipsometry. The interfacial oxide thickness is equivalent to the y-intercept of the line, or by extrapolating the fit back to zero cycles. By fitting the points in Figure 1D we determine a dielectric constant of 20.1 for the deposited ALD film, which meets expectations for a high-quality ALD HfO_2 film.[56] The extrapolated interfacial oxide thickness is ~17 Angstroms, which agrees well with literature.[57] This value is substantially higher than the extracted value from ellipsometry of ~9 Angstroms. We attribute this to the high diffusivity of oxygen in HfO_2, which commonly increases the interfacial oxide thickness during anneals.[58, 59]

Top down and cross section SEM images of the nanowires and nanoplates are shown in Figure 2A. Part 1 of Figure 2A shows an overall top down image of the nanowires. The release window is in the center (highlighted by the yellow arrows) while the metal leads connecting to the nanowires is highlighted by a green arrow. A high magnification image of the nanowires in (1) is shown in Figure 2A(2), where the brighter areas represent the silicon nanowires. The nanowires appear to be ~150nm in width from the top down image in (2), but the cross section in (3) shows them to be ~100nm wide. The cross section in (3) shows the trapezoidal nature of the nanowires from the TMAH anisotropic etch, as well as the surrounding HfO_2 gate dielectric. The thickness of the HfO_2 is approximately 13nm from the image, although it is hard to measure it precisely due to the grain size of the metal sputtering. This thickness agrees well with the thickness information obtained from Figure 1. A top down image for a nanoplate inside the release window is in (4), and shows a nanoplate of ~2um width.

A schematic showing the full cross section of a nanowire and the setup for device testing is in Figure 2B. For fluid testing, a leak free Ag/AgCl reference electrode is biased and swept, with a constant source-drain bias applied. A leak-free reference electrode was chosen since the salt solution encasing the electrode remains constant, helping to minimize drift of the electrode potential during measurements. Incorporating a steady reference electrode is critical in achieving stable measurements with high signal to noise ratio for FET sensing, and has been discussed in literature previously.[60, 61] The back of the handle wafer is grounded, and the Id-Vg transfer curve measured.

The stability of the device under operation in 0.02X SSC buffer is shown in Figure 3. Id-Vg curves were swept from positive to negative bias with the Ag/AgCl electrode and cycled 5 times, shown in Figure 3A. The subthreshold slope extracted for the device is 112mV/decade, comparatively on the low end for nanowire devices in fluid testing. Detailed numerical simulations were performed to validate experiment data (transfer characteristics in Fig. 3a) and to further explore the sensitivity of our devices for pH sensing. In this numerical model, we solve the non-linear Poisson-Boltzmann electrostatics for the sensor system (see Methods section for details). The simulation in Figure 3B show that our detailed numerical simulation interprets the experimental results (red circles) consistently from subthreshold to super-threshold regime. The simulations accurately reproduce experimental transfer curves with the following parameters: Interface trap densities (D_{it}) of 4×10^{11} $cm^{-2}eV^{-1}$, and fixed (negative) charge located at SiO_2/HfO_2 interface with density of ~ 5×10^{11} cm^{-2}. These values of interface trap density are consistent with widely accepted

density of dangling Si bonds at unpassivated Si/SiO_2 interface and the estimate of fixed trap density is also consistent with those reported in literature.[62]

The standard deviation for threshold voltage on the devices is 2.7mV. The combination of a low standard deviation and a low subthreshold slope indicate the combination of a high stability device and low drift reference electrode in electrolytic solutions. Moreover, the fluid is exposed to a ~ 0.2 cm^2 area on the chip, which if not passivated properly would cause leakage current much higher than the measured device current. The leakage throughout this area ranged from 300pA to 1nA, or 1.5 nA/cm^2 to $5nA/cm^2$. An example of long term device stability in 0.02X SSC buffer is shown in Figure 3C. The threshold voltage after each sweep and the time was recorded and repeated over an hour. The change in threshold voltage over time decreases rapidly for the first 10 minutes, then stabilizes. The overall change is 65mV/hour, with only 10mV change happening after the first 10 minutes. In planar ISFETs, the gate voltage instability can be described by a stretched exponential that is characteristic of dispersive transport in disordered materials expressed by:

$$\Delta V_T(t) = \Delta V_{T\infty}\left(1 - \exp\left(\frac{-t}{\tau}\right)^{\beta}\right) \quad (1)$$

where $\Delta V_{T\infty}$ is the maximum V_T change, τ is the time constant, and β is the dispersion parameter that takes a value between $0 < \beta < 1$. As shown in Figure 3C, the theoretical fits according to this model (Eq. 1) agree well with the experimental data. By rearranging Eq. 1 and plotting the natural logarithm *versus* the natural log of time (Figure 3D) we are able to extract the time constant (τ) and the dispersion parameter (β), which are also inset in Figure 3D. The values for $\Delta V_{T\infty}$, β, and τ are 55 mV, 0.7935, and 76.75 seconds, respectively. The standard deviation of the device over 5 sweeps surrounding each time point was also plotted. Briefly, the standard deviation for sweep 15 would include points from sweep 13–17. The standard deviation shows a ~1mV standard deviation per 5 sweeps over the period of the hour. As the device equilibrates, the standard deviation between sweeps goes down. The solid red line indicates the theoretically estimated voltage noise of SiNW pH sensor composed of low-frequency noise and electrolyte noise (See Method section for the details), showing that the sensitivity is limited by the noise from measurement instrument (red triangles), not by the device's intrinsic noise. The leakage to the fluid gate, plotted over the course of an hour, stays relatively stable near 800pA (See Supplementary Figure 1). This indicates little degradation to the HfO_2 dielectric or passivation layer over that time period.

The response and stability of the devices to changes in pH was demonstrated using Robinson buffers for the nanowires and nanoplates. The changes in pH will cause a change in the surface potential on the device due to the proton reactive groups on top of the HfO_2 surface. Robinson buffer solutions ranging from pH's of 4.3–10.5 were used and the threshold voltages of nanowires and nanoplates extracted from the Id-Vg curves. The change in the surface potential with respect to the pH 7.4 solution, set at zero, was plotted *vs.* pH for 3 nanowires and 3 nanoplates, and is shown in Figure 4. We achieve a 55.8 mV/pH sensitivity for the nanowires and 51.0 mV sensitivity for the nanoplates, with the Nernstian limit being 59mV/pH. The sensitivity of nanowires being higher than nanoplates or microwires agrees well with literature[16, 40, 63], as does the range of pH sensitivities found for the HfO_2 sensing dielectric. Our numerical simulations that applied a self-consistent solution of Poisson-Boltzmann electrostatics coupled with OH functional group site-binding model (see Methods section for details) reproduces key experimental trends (line fit in Fig. 4B). Specifically, the model predicts a pH sensitivity of 51mV/pH, which is very close to the experimental results.

The sensing of DNA target was done with different molecular weight PLL functionalizations using the same probe molecule. The procedure for modifying the surface is explained in detail in the Experimental section, but outlined in Figure 5A. Briefly, the poly-l-lysine is electrostatically adsorbed onto the HfO_2 surface and baked on a hotplate at 85°C to ensure a good linkage. Then, the ssDNA probe is electrostatically bound to the HfO_2 surface and excess rinsed off. The ssDNA probe is then baked in order to immobilize it to the poly-l-lysine layer. The target is then hybridized with the probe and sensed on the device. Poly-l-lysine was chosen since it can be deposited from aqueous solution and electrostatically bound to both the HfO_2 and phosphate backbone of probe DNA. This allows for the probe DNA, and binding target, to be in a horizontal conformation.[64] As opposed to a vertical conformation, a horizontal conformation allows for charge density to be closer to the surface, thus creating a larger shift in the surface potential. A horizontal conformation allows for more charge to be felt in the channel at a certain Debye length of electrolyte solution. Other conjugation methods, such as using epoxysilanes with amine modified probes,[65] afforded a lower change in surface potential when depositing the probe in the beginning. The change in surface potential for the probe conjugation was measured both for the epoxysilane and the different molecular weight poly-l-lysines. Both probe conjugations using the different molecular weight poly-l-lysines gave larger surface potential shifts than for the epoxysilane (Supplementary figure 3). Thus, we decided to use and compare the different molecular weight poly-l-lysines for deposition of probes and sensing of target molecules. The sensitivities for the devices with different molecular weight poly-l-lysines are quite different, which we discuss in Figure 7. A lower sensitivity would occur if the overall effective charge density during binding is less, or the charges were farther removed from the surface. A few possibilities which would lead to this are the morphology of the poly-lysine layers as well as the probe density. Thus, we characterized the poly-lysine layers and probe attachment to understand the underlying reasons for this discrepancy.

We used a combination of ellipsometry, AFM, and XPS to look into the morphology, thickness, and probe densities (Table 1). When the PLL layers were deposited, the ellipsometric thicknesses came out to be within error of each other at ~11Å each. This indicates the formation of a polylysine monolayer on the surface. The ssDNA probe attachment came out to be within error as well, at ~20.5 Å each, which leads us to believe the DNA rests in a horizontal configuration. The similar thicknesses for both indicate we should get similar sensitivity levels for target detection.

Thus, we utilized atomic force microscopy (AFM) to characterize the morphology of the 100 cycle ALD HfO_2 layer and the PLL layers. The tapping mode images in Figure 5B are numbered 1–3 in the image set for the untreated HfO_2, PLL (9–14K), and PLL (70–150K), respectively. The images for the untreated HfO_2 and PLL (9–14K) indicate very smooth and uniform layers. The roughness values extracted for the HfO_2 and PLL (9–14K) are 1.1 and 1.6 Å RMS, respectively. The morphology of the PLL (70–150K) is much rougher and has a porous, spongelike appearance. These pores, represented by the darker spotted areas in the image, appear to be the thickness of the monolayer or close to it. Moreover, we were able to determine the thickness of the films by applying a 50nN force to the tip in contact mode and scratching away the PLL layers, then reimaging a larger area in tapping mode. A 50nN force is known to be more than enough to remove organic monolayers and silane layers, without damaging the underlying surface.[66] The images after a 50nN force are 4–6 in the image set. The untreated HfO_2 shows no changes in height, indicating a hard surface. The PLL layers show distinct changes in thickness, indicated by the square scratched area visualized in images 5 and 6. Taking a section analysis across the scratched areas gives us the thickness of the PLL films, and is shown in Figure 5C. The images 4–6 in 5B are color coded to match up with section analyses in Figure 5C. The section analyses showed a similar thickness for

the PLL layers compared to ellipsometry and are in Table 1. However, the buildup of material on the side of the scratched away area was much greater for the lower molecular weight layer (data not shown). This indicates the amount of material for the higher molecular weight PLL on the substrate was less, leaning towards the evidence of a more porous and incomplete layer.

Attachment of the probe DNA to the PLL layers was measured using two techniques: (1) XPS for the P2p peak intensity from the DNA backbone and (2) fluorescence with a Texas Red labeled miR-10b probe. The XPS P2p signal intensity for the HfO_2 and probe DNA on the two PLL layers is in Figure 6A. The peak for the ssDNA on PLL(9–14K) is much larger than the one on PLL (70–150k), indicating a higher probe density. The peak intensities are in Table I, with a ratio of approximately 1.8:1 for the PLL(9–14K):PLL(70–150K). The fluorescently labeled micrographs of bare HfO_2 and PLL layers, both with and without probe are in Figure 6B. The quantification of the fluorescent intensity is in the bar graph in Figure 6C. Images 1 and 2 show the bare HfO_2 layer with and without the probe attachment procedure. The amount of background fluorescence for the HfO_2 with and without probe is about the same. Thus, DNA has very little non-specific adsorption to HfO_2, which should make for better selectivity and less issues with blocking. Images 3 and 4 show the background fluorescence for the PLL layers. The PLL (9–14K) layer shows slightly higher background, as to be expected since there are more optically active surface groups according to AFM. The images for the attachment of the miR-10b probe DNA show slightly greater than a two-fold intensity difference between the PLL layers, with PLL (9–14K) containing the higher probe density. This reaffirms the XPS results in Figure 6A, indicating the probe density is much higher on the lower molecular weight PLL layer.

The demonstration of sensing of miR-10b DNA analogue target on the HfO_2 silicon nanowires is in Figure 7, with the DNA probe and target sequences in Table 2. To make sure the devices were being functionalized properly, Id-Vg curves at key steps during the probe attachment process were taken to examine the changes in threshold voltage (See Supplementary Figure 2)). First, a reference of the bare HfO_2 was taken in the 0.02X SSC sensing buffer. The deposition of PLL then shifts the threshold voltage to the left by ~160mV. The direction of change is proper since the PLL is positively charged and the device operates in accumulation mode, thus creating a more negative threshold to compensate for the positive increase in surface potential. In contrast, when we adsorb the probe DNA we cause a shift in the opposite direction of ~90mV relative to the PLL, which is also expected due to the negative charge density of the phosphate backbone (shifts discussed in more detail in supplementary figure 3). Similar experiments monitoring the adsorption of probe DNA have been performed on nanowires with an 8nm silicon oxide and showed ~250mV shifts from the reference monolayer potential.[67] Since our EOT is lower, the probe DNA density may currently be much less using this PLL based layer and has the potential for further optimization. However, the nanowires and nanoplates in this study did have much greater response than micro-FET's with similar EOT.[68]

After conjugating the ssDNA probe to the PLL surface, various concentrations of miR-10b target were allowed to interact with the sensor for 30 mins (to offer sufficient time for diffusion limited transport down to 100 fM concentration),[69] then rinsed off and Id-Vg curves recorded in the 0.02X SSC sensing buffer. The threshold voltage change with varying target concentrations was then measured relative to the ssDNA probe reference (shown in Figure 7A). The signal-to-noise ratio (SNR) for the measurements was computed and a blue line drawn for 3×SNR, assumed to be the limit of detection for the device. For the lower molecular weight poly-lysine, at least 100fM of miR-10b target was able to be sensed, with an extrapolated limit of detection of 1fM. However, for the higher molecular weight poly-lysine, the limit of detection at 3 × SNR is close to 1nM, close to 6 orders of magnitude

higher. When the mismatch miR-21 target was allowed to hybridize with the miR-10b probe, the signal was very small and steady from 100fM all the way to 1uM concentrations. Most of the miR-21 signals were close to or between 0–5mV change in signal. Error bars for the standard deviation of sweeps over the measurement are also presented on the graph for each case. Similar to the trend in pH sensitivity, nanoplates showed a lower hybridization signal with the miR-10b probe at the same concentrations (see Supplementary Figure 4). For example, the maximum shift for the nanoplate for 1nM DNA concentration with the PLL 9–14K layer was 41mV, while the same shift for a nanowire was 108mV. Similar to the nanowires, the nanoplate also showed the same trend of lower sensitivity with the higher MW PLL layer. The 41mV shift on the microwire mentioned above only afforded a 28mV shift with the PLL 70–150K layer as the probe layer for conjugation. We also found the difference in max potential shifts between the nanowires for the two PLL layers was also greater than it was for the nanoplates. These results for biological detection with nanoplates agree well with the surface potential sensitivity trends presented in Figure 4, as well as the sensitivity difference due to the probe conjugation discussed in Figure 6.

An important feature of the DNA detection sensitivity of NW sensor is that it follows the *logarithmic* dependency on the molecular concentration due to screening by the salt (*i.e.*, $\Delta \Psi_0 \sim \ln(\rho_0)$, where ρ_0 is the DNA concentration).[70] The black solid line represents the corresponding theoretical estimation of $\Delta \Psi_0 = \Psi_{0,0} \times c_1[\ln(\rho_0) - \ln(I_0)/2 + c_2]$ where $c_1 = 4\varepsilon_{ox}k_BT/(q^2 t_{Si}^2 N_A \ln(1+t_{ox}/t_{Si}))$ $\Psi_{0,0}$ and c_2 are parameters that depend on device properties, pH and duration of sensing (*e.g.* 30 min).[65]

The fact that the lower molecular weight PLL shows such higher sensitivity may be attributed to differences in the monolayers. Most important, the overall probe attachment density is much less on the higher molecular weight layer. This will decrease the total amount of binding target, thus causing smaller shifts in surface potential. Moreover, the roughness of the high molecular weight PLL is larger and looks porous compared to the other layer. If the pore sizes are of the width of the nanowires or smaller, this would lead to large void spaces over the nanowire area without probe, making the microscopic amount of probe DNA even less than in the case for a macroscopic image.

Conclusions

In this paper, we have presented a process for the fabrication of HfO_2 based top down silicon nanowires and nanoplates with high stability and robustness in fluid. The ALD process for creating the HfO_2 gate dielectric was thoroughly characterized by ellipsometry, AFM, and CV measurements to assure us of a high quality layer. The devices respond to pH in accordance to sensitivities of other HfO_2 ISFET's, with nanowires slightly more sensitive than plates. Moreover, we characterized the difference between different molecular weight layers of PLL in terms of their surface morphology, thickness, and probe attachment densities. The average thicknesses of the layers were found to be about the same by AFM and ellipsometry, however the probe density of the lower molecular weight PLL was about twice as much as the higher molecular weight one. This was confirmed by both fluorescence and XPS. Moreover, the AFM indicated the higher molecular weight PLL was much rougher and porous, perhaps contributing to the lower response to DNA target using this polymer. Using these different layers for sensing of single stranded DNA oligomers on a nanowire yielded limit of detection differences over 5 orders of magnitude, with the lower molecular weight PLL having higher sensitivity. By using the lower molecular weight poly-l-lysine, we were able to detect down to 100fM of miR-10b DNA analogue with a theoretical limit of detection of 1fM.

Materials and Methods

Materials

All metals for e-beam evaporation were of 99.999% purity and purchased from Lesker Co. DNA and miDNA strands were purchased from Integrated DNA Technologies and purified using HPLC. Poly-l-lysine (PLL) of MW 9,000–14,000 and MW 70,000–150,000 were purchased from Sigma in powder form and used without further purification. Robinson buffer solutions composed of 1mM acetic acid, 1mM phosphoric acid, and 1mM boric acid were titrated with NaOH/HCl from pH's 4–12. All buffer components were purchased from Fisher Scientific. A leak-free Ag/AgCl reference electrode was used to apply bias to the fluid on top of the devices and was purchased from Warner Instruments.

Device Fabrication

A detailed top down fabrication flow has been described previously for creating similar silicon nanoFET devices.[40] The fabrication flow began with bonded Silicon on Insulator (SOI) wafers, doped p-type at $10^{15}/cm^2$ with a buried oxide thickness of 1,450 Å and top silicon thickness of 550 Å. The top silicon was thinned to approximately 300 Angstroms by dry oxidation and stripping of the oxidized layer with 10:1 buffered oxide etch. The wires were then defined via electron beam lithography and wet etched with 25% TMAH to define the active silicon area.[16, 60] The source and drain regions were doped with boron (doping $10^{19}/cm^3$) by ion implantation, and annealed at 1000°C for 5 minutes to active the dopants. The wafer was then dipped in 50:1 BOE for 20s to remove any native oxide, and an SC1/SC2 clean performed. The wafer then underwent a rapid thermal anneal at 1000°C for 60s to help densify the native oxide layer. The HfO_2 gate dielectric was deposited by ALD at a temperature of 120 Celsius for 100 cycles. Following the gate dielectric formation, via holes were etched into the contact regions with 10:1 BOE, and a 100 Å Ni/50 Å TiN layer was deposited in the contact regions by RF sputtering. A rapid thermal anneal was performed at 500°C in Ar to form NiSi and reduce the contact resistance at the source and drain regions of the devices, while also densifying the HfO_2 and creating a wet etch stop. Next, 150nm of Al was sputtered and patterned over the contact areas. A 450°C furnace anneal in Ar/H2 was performed for 30 min to anneal the contacts and remove interface traps in the oxide. Afterwards, a 5,000 Å thick passivation layer of PECVD SiOxNy was deposited over the entire wafer. Metal pad areas on the outside of the Al leads were defined by optical lithography and 10:1 BOE was used to etch the passivation layer. Metal pads composed of 50nm Ti/300nm Ni/500nm Au were then deposited by e-beam evaporation. The final passivation layer etchback to release the HfO_2 devices was done using 10:1 BOE. Subsequently, the wafer is diced (American Precision Dicing) into chips of 1.5×1.5cm for testing.

Materials and Device Characterization

Scanning electron micrographs were taken with a Hitachi S-4800 SEM using secondary electron imaging and an accelerating voltage of 10kV. Before imaging, the samples were sputtered with Au/Pd (80/20)% to minimize charging of the exposed dielectrics and increase topographical contrast. For thickness characterization, HfO_2 of varying thicknesses was deposited by ALD onto polished Si wafers and annealed according to the device fabrication above. The wafer was then covered with photoresist and diced into 1×1cm dies. Ellipsometry measurements were taken using a Rudolph FEIII ellipsometer at a wavelength of 632.8nm and an angle of 70 degrees. Each measurement was taken over ten different areas of a chip and averaged together to get a thickness and standard deviation. For fluorescence measurements, a 1um thick thermal oxide was grown on a polished Si and then 100 cycles ALD HfO_2 deposited on top. The thick oxide was grown in order to limit signal degradation due to fluorescence interference contrast (FLIC).[71] Briefly, FLIC occurs when a

fluorophore is in close contact to a reflecting surface (*i.e.* silicon), and the reflected wavelengths from excitation interact with the emission of the fluorophore, altering its intensity to the detector. To ensure excitation of the fluorophores where the emission will not be largely affected, an oxide greater than the excitation wavelength (for Texas Red, 560–580nm) should be chosen, making 1um of thermal oxide sufficient. The HfO_2 was subsequently annealed according to the device fabrication above. Fluorescent images were taken with a Nikon microscope at an exposure of 800ms and a gain of 1.3x. Atomic force microscopy images of the HfO_2 and PLL layers were taken with an Asylum Cypher AFM using a Force Modulation AFM probe tip (Budget Sensors) with a resonant frequency of 75kHz and a force constant of 1–3 N/m. Force applied to the substrates during contact mode was calibrated by taking the inverse optical lever sensitivity (invOLS) of the cantilever deflection on a bare HfO_2 surface and calculating the spring constant of the cantilever by fitting the thermal fluctuations. X-ray photoelectron spectroscopy of the HfO_2, DNA, and PLL layers were taken with a KRATOS Axis Ultra XPS at a take-off angle of 90 degrees. Survey spectra were acquired at a pass energy of 160eV with 2 sweeps collected. High resolution spectra of Hf4f, P2p, O1s, C1s, and N1s peaks were collected at a pass energy of 40eV with a total of 25 passes per peak.

Electrical measurements

High frequency C-V measurements of HfO_2 MOS capacitors were performed at 1MHz using a Keithley semiconductor parameter analyzer (Keithley 4200) and corrected for series resistance. The capacitors had a top contact of 30nm TiN/100nm Al, and a back contact of 100nm Al, which were DC sputtered. Electrical current measurements and applied biases were controlled by the Keithley 4200 as well. Fluid gate biases were applied with a leak free Ag/AgCl reference electrode (Warner Instruments) that made contact to the solution. Back gate biases were applied using the conductive platform of the probing station which made contact to the backside of the FET dies. At any other times, the conductive platform served as the ground for the FET dies while biases were applied to the fluid gate electrode. The Robinson buffer pH solutions were made using 1 mM acetic, 1 mM phosphoric, and 1 mM boric acid with titrated HCl/NaOH to obtain the desired pH. All pH solutions were measured at the conclusion of the experiment to ensure that the pH had not changed significantly during the course of the experiment.

Preparation of devices for DNA sensing

Before depositing poly-l-lysine, chips were degreased with acetone and methanol, then rinsed in DI water for 1min. The chips then underwent an O_2 plasma at 500mTorr and 200W for 5 minutes. Poly-l-lysine solutions were made to 0.2mg/mL concentration in 5mM $Na_2B_4O_7$, pH 8.5. These conditions were chosen since similar depositions have yielded monolayers for lower MW polymers.[72] Chips are soaked in PLL solution for 2 hours, then taken out of the solution and rinsed in DI water for 1 min. Chips are then blown dry with N_2 and dessicated for 10min. The chips are baked at 85°C in a vacuum oven for 4 hours afterwards.

DNA probe and targets were obtained from Integrated DNA Technologies and diluted to a stock concentration of 100uM in DI water. All stock solutions were stored at −20 Celsius until used. DNA probe solution (10uM in 3X SSC buffer) was spotted on the device in a 10uL volume and allowed to sit for 2 hours in a humidity chamber. The chip was then rinsed in 2X SSC, 0.2X SSC, and 5% EtOH for 1 min each, and blown dry with N2. To crosslink the DNA to the PLL, chips were baked at 85°C for 2 hours in a convection oven. A PDMS well with an adhesive bottom tape was attached to the chip afterwards. Each well had a circular diameter of 5mm and a fluid volume of ~50uL. The target solutions for varying concentrations of miR-10b and miR-21 were made in 2X SSC buffer and put in the PDMS

well for 30 mins to hybridize. The target was then rinsed off 3 times in 2X SSC buffer and 3 times in 0.2X SSC buffer before measuring in 0.02X SSC buffer.

Theoretical Model for pH response and noise of SiNW sensor

The sensitivity of ISFET to pH fluctuations in the buffer is determined by the protonation/de-protonation kinetics of –OH functional groups at the gate oxide-electrolyte interface and the electrostatics of the system,[5, 73, 74] as described by the equations in Table 2. For reaction kinetics of –OH functional groups, we use the site binding model[75] with reasonably calibrated parameters (N_s, K_a, and pK_b in Table 3) regarding HfO_2 surface due to unavailability of experimentally observed values in the literature. The electrostatics for the rest of the system (electrolyte, gate oxide, and Si) follows the Poisson-Boltzmann equations with given concentration, dielectric constant, and boundary conditions. The model equations in Table 3 are discretized using finite difference scheme and self-consistently solved using Newton iteration due to the strong non-linear nature of the equations.[76] For the relevant device dimensions used in our experiments (t_{Si} ~55nm, t_{ox}~4nm), the cylindrical gate oxide capacitance, $C_{cylind}=2\varepsilon_{ox}/(t_{Si}\times\ln(1+2t_{ox}/t_{Si}))$ is comparable to the corresponding planar gate oxide capacitance, $C_{cylind}=\varepsilon_{ox}/t_{ox}$. This allows us to reduce the computational complexity and solve the system of equations for the equivalent planar system. We assume Boltzmann distribution for the ions in the electrolyte and long channel with small drain bias to simply estimate the conductance of Si channel.

For the theoretical estimation of voltage noise in ISFET, we consider two major sources of noise: low frequency $1/f$ noise ($\delta V_{1/f}$) and the electrolyte noise (δV_e), as summarized in Table 4.[77] Each noise term is obtained by integrating the corresponding power spectral density ($S_{V_{FB}}$ for 1/f noise and S_{V_e} for electrolyte noise) in a given frequency range ($f_1<f<f_2$). We assume the noise sources are uncorrelated thus the total noise of ISFET pH sensor (illustrated as the horizontal dashed line in Fig. 3C) is given by $\delta V=\sqrt{\delta V_{1/f}^2+\delta V_e^2}$.

Supplementary Material

Refer to Web version on PubMed Central for supplementary material.

Acknowledgments

We would like to acknowledge the use of the Micro and Nanotechnology Laboratory at UIUC for FET processing, and the Materials Research Laboratory at UIUC for materials characterization. B.R.D. is a trainee supported by the Midwestern Cancer Nanotechnology Training Center (NIH-NCI R25 CA154015) at UIUC. We would also like to acknowledge support from NIH R01-CA20003 and National Science Foundation (NSF) Grant EEC-0425626 (NSF Nanoscale Science and Engineering Center at Ohio State University). J.-H.G and M.A.A. acknowledge financial support from MSD Focus Center and computational resources from the Network of computational nanotechnology.

References

1. Harvey MA. Point-of-Care Laboratory Testing in Critical Care. Am J Crit Care. 1999; 8:72–83. [PubMed: 10071697]
2. Kilgore ML, Steindel SJ, Smith JA. Evaluating Stat Testing Options in an Academic Health Center: Therapeutic Turnaround Time and Staff Satisfaction. Clin Chem. 1998; 44:1597–1603. [PubMed: 9702944]
3. Douketis JD. Patient Self-Monitoring of Oral Anticoagulant Therapy: Potential Benefits and Implications for Clinical Practice. American journal of cardiovascular drugs: drugs, devices, and other interventions. 2001; 1:245–251.
4. Price CP. Regular Review: Point of Care Testing. Br Med J. 2001; 322:1285–1288. [PubMed: 11375233]

5. Bergveld P. Thirty Years of Isfetology: What Happened in the Past 30 Years and What May Happen in the Next 30 Years. Sensors and Actuators, B: Chemical. 2003; 88:1–20.
6. Kimura J, Kuriyama T. Fet Biosensors. J Biotechnol. 1990; 15:239–254. [PubMed: 1366677]
7. Lee CS, Kyu Kim S, Kim M. Ion-Sensitive Field-Effect Transistor for Biological Sensing. Sensors. 2009; 9:7111–7131. [PubMed: 22423205]
8. Sandifer JR, Voycheck JJ. A Review of Biosensor and Industrial Applications of Ph-Isfets and an Evaluation of Honeywell's "Durafet". Mikrochim Acta. 1999; 131:91–98.
9. Schöning MJ, Poghossian A. Bio Feds (Field-Effect Devices): State-of-the-Art and New Directions. Electroanalysis. 2006; 18:1893–1900.
10. Yuqing M, Jianguo G, Jianrong C. Ion Sensitive Field Effect Transducer-Based Biosensors. Biotechnol Adv. 2003; 21:527–534. [PubMed: 14499153]
11. Patolsky F, Zheng GF, Lieber CM. Fabrication of Silicon Nanowire Devices for Ultrasensitive, Label-Free, Real-Time Detection of Biological and Chemical Species. Nature Protocols. 2006; 1:1711–1724.
12. Zheng GF, Patolsky F, Cui Y, Wang WU, Lieber CM. Multiplexed Electrical Detection of Cancer Markers with Nanowire Sensor Arrays. Nat Biotechnol. 2005; 23:1294–1301. [PubMed: 16170313]
13. Cui Y, Wei QQ, Park HK, Lieber CM. Nanowire Nanosensors for Highly Sensitive and Selective Detection of Biological and Chemical Species. Science. 2001; 293:1289–1292. [PubMed: 11509722]
14. Stern E, Vacic A, Rajan NK, Criscione JM, Park J, Ilic BR, Mooney DJ, Reed MA, Fahmy TM. Label-Free Biomarker Detection from Whole Blood. Nature Nanotechnology. 2010; 5:138–142.
15. Stern E, Vacic A, Li C, Ishikawa FN, Zhou CW, Reed MA, Fahmy TM. A Nanoelectronic Enzyme-Linked Immunosorbent Assay for Detection of Proteins in Physiological Solutions. Small. 2010; 6:232–238. [PubMed: 19882688]
16. Stern E, Klemic JF, Routenberg DA, Wyrembak PN, Turner-Evans DB, Hamilton AD, LaVan DA, Fahmy TM, Reed MA. Label-Free Immunodetection with Cmos-Compatible Semiconducting Nanowires. Nature. 2007; 445:519–522. [PubMed: 17268465]
17. Li Z, Chen Y, Li X, Kamins TI, Nauka K, Williams RS. Sequence-Specific Label-Free DNA Sensors Based on Silicon Nanowires. Nano Lett. 2004; 4:245–247.
18. Hahm J, Lieber CM. Direct Ultrasensitive Electrical Detection of DNA and DNA Sequence Variations Using Nanowire Nanosensors. Nano Lett. 2004; 4:51–54.
19. Fritz J, Cooper EB, Gaudet S, Sorger PK, Manalis SR. Electronic Detection of DNA by Its Intrinsic Molecular Charge. Proc Natl Acad Sci U S A. 2002; 99:14142–14146. [PubMed: 12386345]
20. Gao A, Lu N, Dai P, Li T, Pei H, Gao X, Gong Y, Wang Y, Fan C. Silicon-Nanowire-Based Cmos-Compatible Field-Effect Transistor Nanosensors for Ultrasensitive Electrical Detection of Nucleic Acids. Nano Lett. 2011; 11:3974–3978. [PubMed: 21848308]
21. Zhang GJ, Chua JH, Chee RE, Agarwal A, Wong SM. Label-Free Direct Detection of Mirnas with Silicon Nanowire Biosensors. Biosensors Bioelectron. 2009; 24:2504–2508.
22. Luo L, Jie J, Zhang W, He Z, Wang J, Yuan G, Wu LCM, Lee ST. Silicon Nanowire Sensors for Hg2+ and Cd2+ Ions. Appl Phys Lett. 2009:94.
23. Wang WU, Chen C, Lin KH, Fang Y, Lieber CM. Label-Free Detection of Small-Molecule-Protein Interactions by Using Nanowire Nanosensors. Proc Natl Acad Sci U S A. 2005; 102:3208–3212. [PubMed: 15716362]
24. Elibol OH, Morisette D, Akin D, Denton JP, Bashir R. Integrated Nanoscale Silicon Sensors Using Top-Down Fabrication. Appl Phys Lett. 2003; 83:4613–4615.
25. Kim A, Ah CS, Yu HY, Yang JH, Baek IB, Ahn CG, Park CW, Jun MS, Lee S. Ultrasensitive, Label-Free, and Real-Time Immunodetection Using Silicon Field-Effect Transistors. Appl Phys Lett. 2007:91.
26. Choi S, Park I, Hao Z, Holman HYN, Pisano AP. Quantitative Studies of Long-Term Stable, Top-Down Fabricated Silicon Nanowire Ph Sensors. Applied Physics A: Materials Science and Processing. 2012:1–8.

27. Ginet P, Akiyama S, Takama N, Fujita H, Kim B. Cmos-Compatible Fabrication of Top-Gated Field-Effect Transistor Silicon Nanowire-Based Biosensors. Journal of Micromechanics and Microengineering. 2011:21.
28. Park I, Li Z, Pisano AP, Williams RS. Top-Down Fabricated Silicon Nanowire Sensors for Real-Time Chemical Detection. Nanotechnology. 2010:21.
29. Tong HD, Chen S, Van Der Wiel WG, Carlen ET, Van Berg AD. Novel Top-Down Wafer-Scale Fabrication of Single Crystal Silicon Nanowires. Nano Lett. 2009; 9:1015–1022. [PubMed: 19199755]
30. Chen S, Bomer JG, Van der Wiel WG, Carlen ET, Van Den Berg A. Top-Down Fabrication of Sub-30 Nm Monocrystalline Silicon Nanowires Using Conventional Microfabrication. ACS Nano. 2009; 3:3485–3492. [PubMed: 19856905]
31. Chen S, Nyholm L, Jokilaakso N, Karlstrm AE, Linnros J, Smith U, Zhang SL. Current Instability for Silicon Nanowire Field-Effect Sensors Operating in Electrolyte with Platinum Gate Electrodes. Electrochem Solid-State Lett. 2011; 14:J34–J37.
32. Kim S, Kim K, Rim T, Park C, Cho D, Baek CK, Jeong YH, Meyyappan M, Lee JS. Ph Sensing and Noise Characteristics of Si Nanowire Ion-Sensitive Field Effect Transistors. 2011:1233–1236.
33. Lu MP, Hsiao CY, Lai WT, Yang YS. Probing the Sensitivity of Nanowire-Based Biosensors Using Liquid-Gating. Nanotechnology. 2010:21.
34. Rajan NK, Routenberg DA, Chen J, Reed MA. Temperature Dependence of 1/F Noise Mechanisms in Silicon Nanowire Biochemical Field Effect Transistors. Applied Physics Letters. 2010:97.
35. Zemel JN. Microfabricated Nonoptical Chemical Sensors. Rev Sci Instrum. 1990; 61:1579–1606.
36. Bousse L, Bergveld P. The Role of Buried Oh Sites in the Response Mechanism of Inorganic-Gate Ph-Sensitive Isfets. Sensors and Actuators. 1984; 6:65–78.
37. Chen S, Bomer JG, Carlen ET, Van Den Berg A. Al2o3/Silicon Nanoisfet with near Ideal Nernstian Response. Nano Lett. 2011; 11:2334–2341. [PubMed: 21526845]
38. Zafar S, D'Emic C, Afzali A, Fletcher B, Zhu Y, Ning T. Optimization of Ph Sensing Using Silicon Nanowire Field Effect Transistors with Hfo2 as the Sensing Surface. Nanotechnology. 2011:22.
39. Rothberg JM, Hinz W, Rearick TM, Schultz J, Mileski W, Davey M, Leamon JH, Johnson K, Milgrew MJ, Edwards M, et al. An Integrated Semiconductor Device Enabling Non-Optical Genome Sequencing. Nature. 2011; 475:348–352. [PubMed: 21776081]
40. Reddy B Jr, Dorvel BR, Go J, Nair PR, Elibol OH, Credo GM, Daniels JS, Chow EKC, Su X, Varma M, et al. High-K Dielectric Al2o3 Nanowire and Nanoplate Field Effect Sensors for Improved Ph Sensing. Biomed Microdevices. 2011; 13:335–344. [PubMed: 21203849]
41. Robertson J. High Dielectric Constant Oxides. European Physical Journal-Applied Physics. 2004; 28:265–291.
42. Lai CS, Yang CM, Lu TF. Ph Sensitivity Improvement on 8 Nm Thick Hafnium Oxide by Post Deposition Annealing. Electrochem Solid-State Lett. 2006; 9:G90–G92.
43. Van Der Wal PD, Briand D, Mondin G, Jenny S, Jeanneret S, Millon C, Roussel H, Dubourdieu C, De Rooij NF. High-K Dielectrics for Use as Isfet Gate Oxides. 2004:677–680.
44. Chen YW, Liu M, Kaneko T, McIntyre PC. Atomic Layer Deposited Hafnium Oxide Gate Dielectrics for Charge-Based Biosensors. Electrochem Solid-State Lett. 2010; 13:G29–G32.
45. Gabriely G, Teplyuk NM, Krichevsky AM. Context Effect: Microrna-10b in Cancer Cell Proliferation, Spread and Death. Autophagy. 2011; 7:1384–1386. [PubMed: 21795860]
46. Iyevleva AG, Kuligina ES, Mitiushkina NV, Togo AV, Miki Y, Imyanitov EN. High Level of Mir-21, Mir-10b, and Mir-31 Expression in Bilateral *Vs.* Unilateral Breast Carcinomas. Breast Cancer Res Treat. 2012; 131:1049–1059. [PubMed: 22057972]
47. Ma L, Reinhardt F, Pan E, Soutschek J, Bhat B, Marcusson EG, Teruya-Feldstein J, Bell GW, Weinberg RA. Therapeutic Silencing of Mir-10b Inhibits Metastasis in a Mouse Mammary Tumor Model. Nat Biotechnol. 2010; 28:341–347. [PubMed: 20351690]
48. Ma L, Teruya-Feldstein J, Weinberg RA. Tumour Invasion and Metastasis Initiated by Microrna-10b in Breast Cancer. Nature. 2007; 449:682–688. [PubMed: 17898713]

49. Cissell KA, Rahimi Y, Shrestha S, Hunt EA, Deo SK. Bioluminescence-Based Detection of Microrna, Mir21 in Breast Cancer Cells. Anal Chem. 2008; 80:2319–2325. [PubMed: 18302417]
50. Liang Y, Ridzon D, Wong L, Chen C. Characterization of Microrna Expression Profiles in Normal Human Tissues. BMC Genomics. 2007:8. [PubMed: 17210083]
51. Hausmann DM, Kim E, Becker J, Gordon RG. Atomic Layer Deposition of Hafnium and Zirconium Oxides Using Metal Amide Precursors. Chem Mater. 2002; 14:4350–4358.
52. Kukli K, Ritala M, Sajavaara T, Keinonen J, Leskelä M. Atomic Layer Deposition of Hafnium Dioxide Films from Hafnium Tetrakis(Ethylmethylamide) and Water. Chem Vap Deposition. 2002; 8:199–204.
53. Bohra F, Jiang B, Zuo JM. Textured Crystallization of Ultrathin Hafnium Oxide Films on Silicon Substrate. Appl Phys Lett. 2007:90.
54. Wilk GD, Wallace RM, Anthony JM. Hafnium and Zirconium Silicates for Advanced Gate Dielectrics. J Appl Phys. 2000; 87:484–492.
55. Nicollian, EH.; JRB. Mos Physics and Technology. Wiley; New York, NY: 1982.
56. Callegari A, Cartier E, Gribelyuk M, Okorn-Schmidt HF, Zabel T. Physical and Electrical Characterization of Hafnium Oxide and Hafnium Silicate Sputtered Films. J Appl Phys. 2001; 90:6466–6475.
57. Zhong L, Daniel WL, Zhang Z, Campbell SA, Gladfelter WL. Atomic Layer Deposition, Characterization, and Dielectric Properties of Hfo2/Sio2 Nanolaminates and Comparisons with Their Homogeneous Mixtures. Chem Vap Deposition. 2006; 12:143–150.
58. Goncharova LV, Dalponte M, Feng T, Gustafsson T, Garfunkel E, Lysaght PS, Bersuker G. Diffusion and Interface Growth in Hafnium Oxide and Silicate Ultrathin Films on Si(001). Physical Review B - Condensed Matter and Materials Physics. 2011:83.
59. Rudenja S, Minko A, Buchanan DA. Low-Temperature Deposition of Stoichiometric Hfo2 on Silicon: Analysis and Quantification of the Hfo2/Si Interface from Electrical and Xps Measurements. Appl Surf Sci. 2010; 257:17–21.
60. Vu XT, Eschermann JF, Stockmann R, Ghoshmoulick R, Offenhäusser A, Ingebrandt S. Top-Down Processed Silicon Nanowire Transistor Arrays for Biosensing. Physica Status Solidi (A) Applications and Materials Science. 2009; 206:426–434.
61. Vu XT, Stockmann R, Wolfrum B, Offenhäuser A, Ingebrandt S. Fabrication and Application of a Microfluidic-Embedded Silicon Nanowire Biosensor Chip. Physica Status Solidi (A) Applications and Materials Science. 2010; 207:850–857.
62. Fleetwood DM, Winokur PS, Reber RA Jr, Meisenheimer TL, Schwank JR, Shaneyfelt MR, Riewe LC. Effects of Oxide Traps, Interface Traps, and “Border Traps” on Metal-Oxide-Semiconductor Devices. J Appl Phys. 1993; 73:5058–5074.
63. Elfström N, Juhasz R, Sychugov I, Engfeldt T, Karlström AE, Linnros J. Surface Charge Sensitivity of Silicon Nanowires: Size Dependence. Nano Lett. 2007; 7:2608–2612. [PubMed: 17691849]
64. Saprigin AV, Thomas CW, Dulcey CS, Patterson CH Jr, Spector MS. Spectroscopic Quantification of Covalently Immobilized Oligonucleotides. Surf Interface Anal. 2005; 37:24–32.
65. Protocol from Schott Nexterion for DNA Microarray Epoxysilane Slide E. http://www.us.schott.com/nexterion/english/download/protocol_slide_e_1_3_us.pdf
66. Crampton N, Bonass WA, Kirkham J, Thomson NH. Formation of Aminosilane-Functionalized Mica for Atomic Force Microscopy Imaging of DNA. Langmuir. 2005; 21:7884–7891. [PubMed: 16089396]
67. Vu XT, GhoshMoulick R, Eschermann JF, Stockmann R, Offenhäusser A, Ingebrandt S. Fabrication and Application of Silicon Nanowire Transistor Arrays for Biomolecular Detection. Sensors and Actuators, B: Chemical. 2010; 144:354–360.
68. Ingebrandt S, Offenhäusser A. Label-Free Detection of DNA Using Field-Effect Transistors. Physica Status Solidi (A) Applications and Materials Science. 2006; 203:3399–3411.
69. Nair PR, Alam MA. Performance Limits of Nanobiosensors. Appl Phys Lett. 2006; 88
70. Nair PR, Alam MA. Screening-Limited Response of Nanobiosensors. Nano Lett. 2008; 8:1281–1285. [PubMed: 18386914]

71. Lambacher A, Fromherz P. Fluorescence Interference-Contrast Microscopy on Oxidized Silicon Using a Monomolecular Dye Layer. Applied Physics a-Materials Science & Processing. 1996; 63:207–216.

72. Jordan CE, Frey BL, Kornguth S, Corn RM. Characterization of Poly-L-Lysine Adsorption onto Alkanethiol-Modified Gold Surfaces with Polarization-Modulation Fourier Transform Infrared Spectroscopy and Surface Plasmon Resonance Measurements. Langmuir. 1994; 10:3642–3648.

73. Landheer D, McKinnon WR, Aers G, Jiang W, Deen MJ, Shinwari MW. Calculation of the Response of Field-Effect Transistors to Charged Biological Molecules. IEEE Sens J. 2007; 7:1233–1241.

74. Landheer D, Aers G, McKinnon WR, Deen MJ, Ranuarez JC. Model for the Field Effect from Layers of Biological Macromolecules on the Gates of Metal-Oxide-Semiconductor Transistors. J Appl Phys. 2005:98.

75. Yates DE, Levine S, Healy TW. Site-Binding Model of the Electrical Double Layer at the Oxide/Water Interface. Journal of the Chemical Society, Faraday Transactions 1: Physical Chemistry in Condensed Phases. 1974; 70:1807–1818.

76. Go J, Nair PR, Reddy B Jr, Dorvel B, Bashir R, Alam MA. Beating the Nernst Limit of 59mv/Ph with Double-Gated Nano-Scale Field-Effect Transistors and Its Applications to Ultra-Sensitive DNA Biosensors. 2010:8.7.1–8.7.4.

77. Deen MJ, Shinwari MW, Ranuárez JC, Landheer D. Noise Considerations in Field-Effect Biosensors. J Appl Phys. 2006:100.

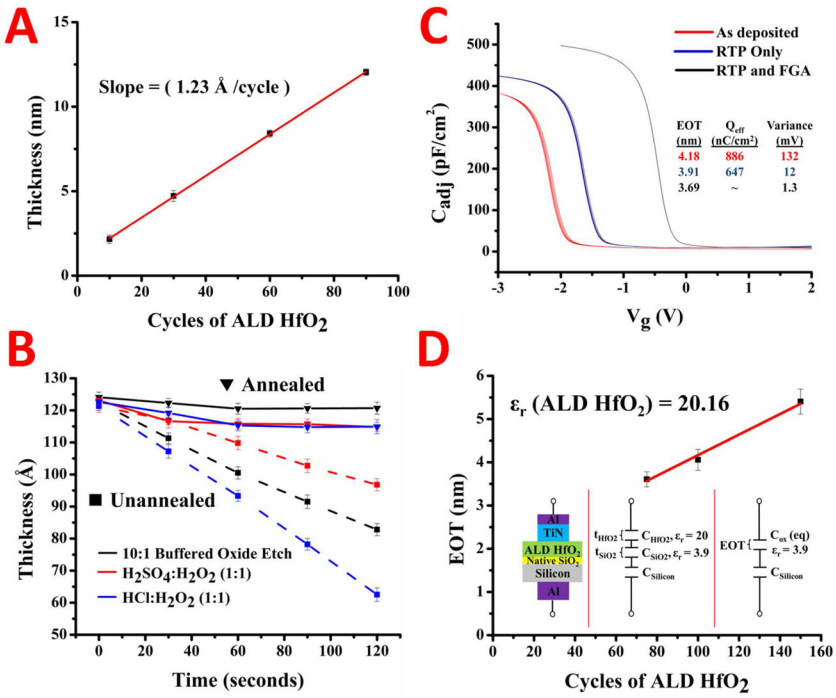

Figure 1.

Characterization of the HfO_2 gate dielectric deposited by atomic layer deposition. The thickness of HfO_2 *versus* the amount of ALD cycles is shown in **A** with the slope inset. The effect of annealing the HfO_2 against chemical etchants is shown in **B** with the ellipsometric thickness *versus* etching time. High frequency capacitance-voltage curves for varying steps in the annealing procedure are in **C** with extracted values inset. The equivalent oxide thickness extracted from the C-V analysis *versus* the ALD cycle amount is plotted in **D** with the extracted dielectric constant inset.

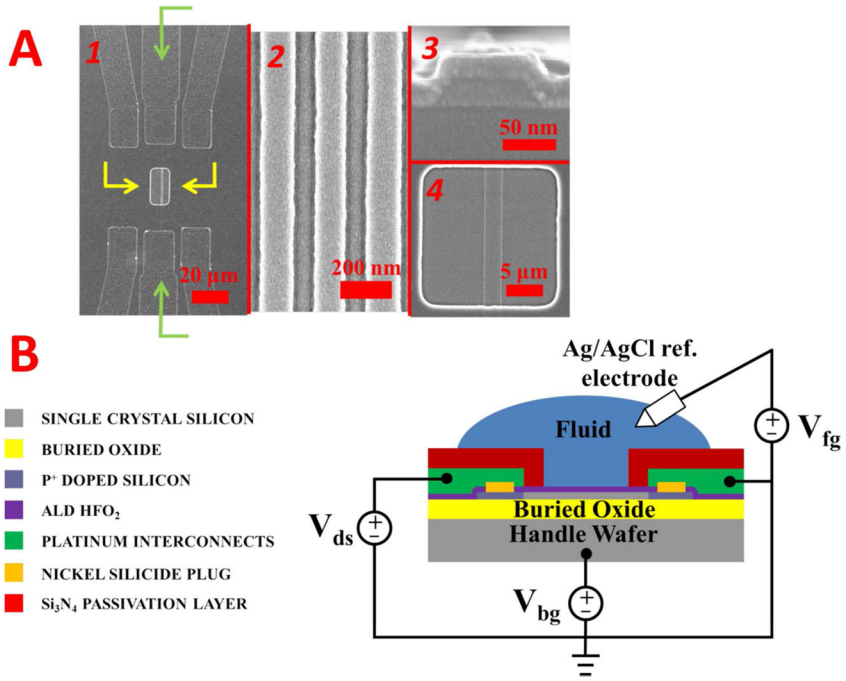

Figure 2.

Scanning electron micrographs of the silicon nanowires are in **A**. Image 1 shows an overview of the nanowire sensing area, with the source-drain metal leads (green arrows) and release window (yellow arrows) highlighted. A high magnification top-down image of the nanowires is shown in 2. A cross-sectional image of a nanowire is in 3 while a top down image a nanoplate is in 4. A horizontal cross sectional schematic of sensing setup is represented in **B**. The relevant structures are color coded to the left, with an example electrical measurement setup for the source drain (V_{ds}), fluid gate (V_{fg}), and back gate (V_{bg}).

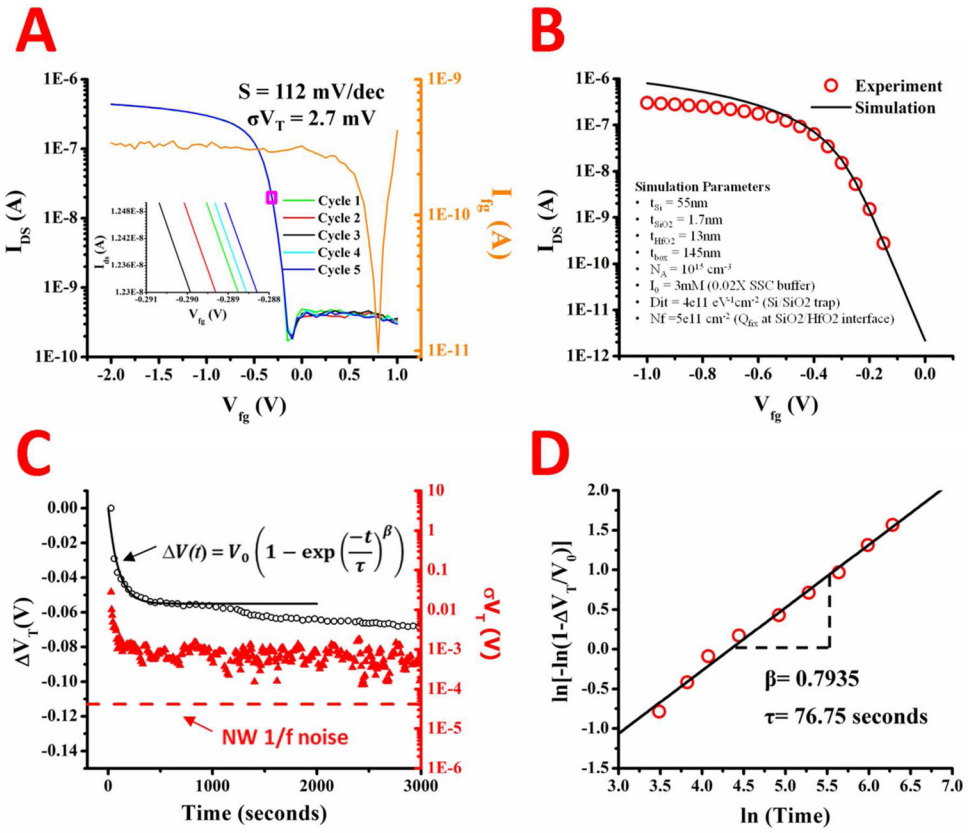

Figure 3.

Representative source-drain current verse fluid gate voltage for a nanowire is shown in **A**. The nanowires were swept for 5 cycles with the fluid gate leakage also measure (right side of graph) and an enlarged view of the curve repeatability is inset in **A**. The numerical simulation (black line) of the average of the experimental transfer curves in **A** (red circles) is shown in **B** with the simulation parameters (inset). The change in the threshold voltage (left side) and standard deviation in threshold (right side) *versus* time for a nanowire is in **C**. The equation for modeling the gate voltage instability is inset in C, with the fit to the experimental data represented as the black line. The theoretically estimated low frequency voltage noise is represented as a dashed red line. The experimental ΔVt data in **C** was rearranged according to the equation in **C** to extract the time constant and dispersion parameter. The natural log of the rearrangement is plotted in **D** *versus* the natural log of the time (red circles), with the linear fit to the data (black line) and the extracted parameters (inset).

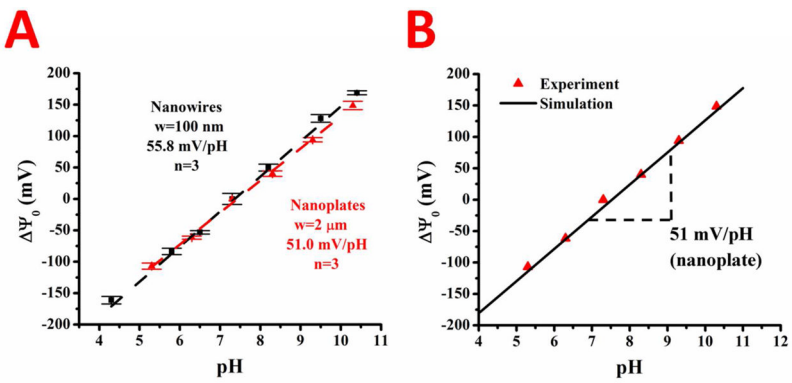

Figure 4.

The change in surface potential of the HfO_2 sensing dielectric *versus* solution pH for nanowires (black) and nanoplates (red) is shown in **A**. The pH sensitivity for nanowires and nanoplates was extracted through linear regression and is displayed inset. Numerical simulations (black line) of the nanoplate data (red triangles) using self-consistent Poisson-Boltzmann electrostatics and an OH group site binding model is shown in **B**, with the extracted pH sensitivity inset.

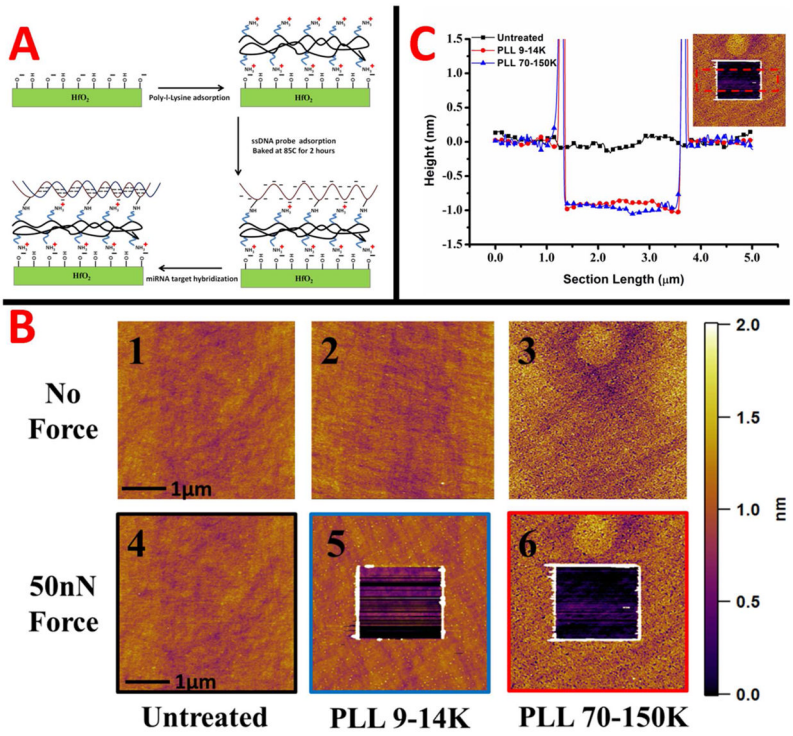

Figure 5.

A schematic of the surface functionalization of the HfO_2 surface for microRNA (DNA analogue) sensing is shown in **A**. AFM images of the HfO_2 and poly-l-lysine layers of different molecular weights are shown in **B**. Tapping mode images with no force applied (upper) for the different layers, and after a 50nN scratching force (bottom) are displayed. The scale bar for all AFM images is on the right. A cross section for the images with 50nN force applied is in part **C**. The cross sections are color coded to images in **B** with an inset representing the cross sectional area.

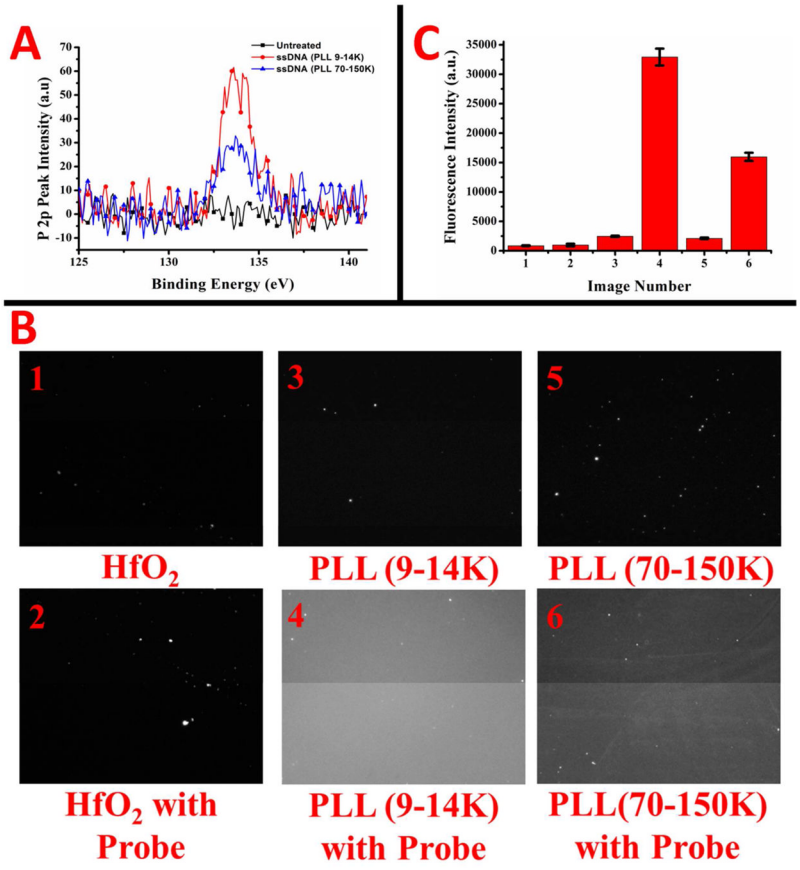

Figure 6.

P2p peak intensities from XPS are shown in **A** for ssDNA adsorption onto the poly-l-lysine layers of different molecular weights, and onto the bare HfO2 surface. Fluorescent micrographs of ssDNA probe immobilization are shown in **B** for HfO2 and the different molecular weight poly-l-lysines, both with and without exposure to ssDNA probe. Fluorescent intensities for images 1–6 in **B** are plotted in column format in **C**.

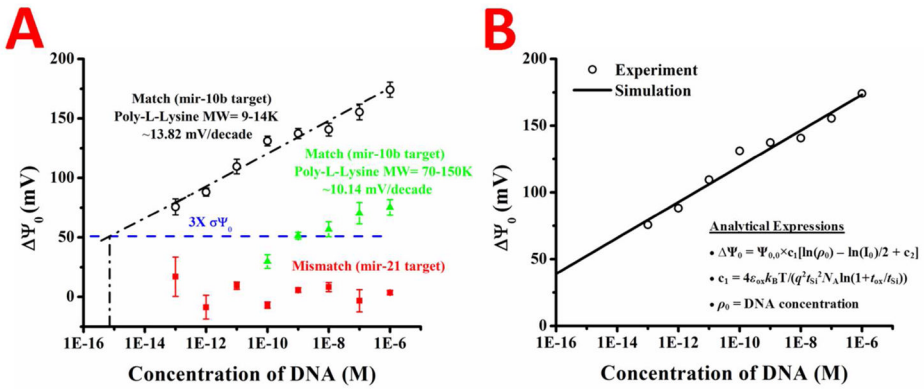

Figure 7.

The change in surface potential *versus* the concentration of target in solution is plotted in **A** for the two different poly-l-lysines, with the slopes of the respective lines calculated. The change in surface potential for the mismatched target is shown to be negligible (red squares) and a theoretical limit of detection line is drawn in blue. The linear regression for the PLL (9–14K) is shown in **A** (black dashed line) and extrapolated to the theoretical limit of detection line. The change in surface potential *versus* the DNA concentration for the PLL (9–14K) data was also theoretically calculated, and is shown in **B**. The change in the surface potential (black circles) matches the theoretical prediction (black line) well. The analytical expressions used for the calculation are inset in **B**. The parameters used in the theoretical calculation of $\Delta \Psi_0$ are: t_{Si} = 55nm, t_{ox} (EOT) = 4.22nm, $N_A = 10^{15}cm^{-3}$, and I_0 = 3mM. The device specific parameters are $\Psi_{0,0}$ = 58.3mV and c_2=40.63.

Table 1

Characterization of the thickness, roughness, and probe density of the HfO_2 surface functionalization process.

	Ellipsometric Thickness (Å)	AFM Thickness (Å)	Roughness (Å)	XPS P 2p Peak Area
HfO_2 layer	120.1 ± 3.2	–	1.1	–
PLL 9–14K	11.3 ± 1.5	11.2	1.6	–
PLL 70–150K	12.1 ± 2.1	9.8	3.4	–
ssDNA (PLL 9–14K)	21.6 ± 2.3	–	1.9	145.7
ssDNA (PLL 70–150K)	19.8 ± 2.7	–	2.9	74.2

Table 2

Nucleic acid sequences for the immobilized probe and DNA targets

	Sequence
DNA probe	5′-CACAAATTCGGTTCTACAGGGTA-3′
miR-10b DNA complementary target	5′-TACCCTGTAGAACCGAATTTGTG-3′
miR-21 DNA non-complementary target	5′-TAGCTTATCAGACTGATGTTGA-3′

Table 3

Model equations of ISFET electrostatics

Region	Model Equations	Description of variables
Electrolyte	Poisson-Boltzmann Equation $-\nabla(\varepsilon_w \nabla\psi) = -2qn_0 \sinh(q(\psi - V_{FG})/k_B T)$	n_0-buffer ion concentration (3mM, corresponding to 0.02X SSC buffer), V_{FG}: fluid gate bias k_B: Boltzmann constant, T-Temperature
Gate dielectric-electrolyte interface	Protonation/de-protonation of OH groups $AOH \leftrightarrow AO^- + H_s^+$ $AOH_2^+ \leftrightarrow AOH + H_s^+$ OH surface density $N_s = [AOH] + [AO^-] + [AOH_2^+]$ Reaction constants $K_a = \frac{[AO^-][H_s^+]}{[AOH]}$ $K_b = \frac{[AOH][H_s^+]}{[AOH_2^+]}$ Boundary condition $(\varepsilon_{ox} \nabla\psi\|_{0^-}) - (\varepsilon_w \nabla\psi\|_{0^+}) = q([AOH_2^+] - [AO^-])$	H_s^+ − H^+ concentration at gate-oxide/electrolyte interface. H_b^+: H^+ concentration at the bulk electrolyte. $H_s^+ = H_b^+ e^{-\frac{q\psi}{k_B T}}$ $pH = -\log_{10}(H_b^+)$ N_s = 8e14 cm^{-2} for HfO_2 $pK_a = -\log_{10}(K_a)$, $pK_b = -\log_{10}(K_b)$ (pK_a, pK_b) = (6, 10) for HfO_2 ε_w =80 ε_0,
Gate dielectric	Poisson Equation $-\nabla(\varepsilon_{ox} \nabla\psi) = 0$ (Acceptor like interface traps (D_{it}) are assumed at Si/Gate oxide interface. For SiO_2/HfO_2 gate oxide stack, a fixed interface charge is assumed.)	ε_{ox} = 3.9ε_0 (SiO_2) or 20.1 ε_0 (HfO_2) D_{it}: interface trap density at Si/Gate dielectric interface ($D_{it} \sim 4\times10^{11} cm^{-2}/eV$). Q_F: fixed charge density at SiO_2/HfO_2 interface.
Si	Poisson Equation $-\nabla(\varepsilon_{si} \nabla\psi) = q(p - n - N_A)$ $p = n_i e^{-q(\psi - \psi_f)/k_B T}$, $n = n_i e^{q(\psi - \psi_f)/k_B T}$	ψ-electrostatic potential, ε_{si} = 11.9ε_0, ε_0 dielectric permittivity of vaccum, q-electronic charge, N_A-doping of Si (10^{15} cm^{-3}), ψ_f = Fermi level in Si.

Table 4

Model equations for noise estimation

Region	Model Equations	Description of Variables
Si-NW	Low-frequency voltage noise $\delta V_{1/f} = \sqrt{\int_{f_1}^{f_2} S_{V_{FB}} df} = \sqrt{\frac{q^2 k_B T N_t \lambda}{WLC_{eff}^2} \ln \frac{f_2}{f_1}}$ $S_{V_{FB}} = \frac{q^2 k_B T N_t \lambda}{fWLC_{eff}^2}$ where (Acceptor like interface traps (D_{it}) are assumed at Si/Gate oxide interface. For SiO_2/HfO_2 gate oxide stack, a fixed interface charge is assumed.)	$W = 0.1\ \mu$m, $L = 20\ \mu$m $f_1 = 1$Hz, $f_2 = 1$kHz (f_1, f_2: low and high cutoff frequency) $\alpha = 1.5\times10^5$ V s/C (Coulomb scattering coefficient) $\lambda = 0.5$ Å (tunneling parameter) $N_t = 3\times10^{16}\text{eV}^{-1}\ \text{cm}^{-3}$, (trap density) $C_{eff} = (1/C_{SiO2}+1/C_{HfO2})^{-1} = 8.17\times10^{-7}$ F/cm^2 T=300K
Electrolyte	Electrolyte bulk resistance $\delta V_e = \sqrt{\int_{f_1}^{f_2} S_{V_e} df} = \sqrt{4k_B T R_b (f_2 - f_1)}$ where $S_{V_e}=4k_BTR_b$s and $R_b \sqrt{\pi/WL}/\kappa$	$\kappa = 0.124\times10^{-3}$ S/cm (electrolyte conductivity), k_B: Boltzmann constant, T-Temperature